

Electrochemical characterisations to elucidate the pseudocapacitance mechanisms of a CdS/WO_x nanocomposite photoanode in acidic aqueous electrolytes

Daniel R. Jones^{a*} and Charles W. Dunnill^a

^aEnergy Safety Research Institute (ESRI), Swansea University Bay Campus, Swansea SA1 8EN, UK

*Email: D.R.Jones@swansea.ac.uk

Abstract

The electrochemical properties of a cadmium sulphide/tungsten(VI) sub-oxide (CdS/WO_x) nanocomposite have been explored using aqueous solutions of acetic acid (pH 2.2) and acidified sodium acetate (pH 5.0), for the purpose of evaluating the origin of pseudocapacitance within the material. Through transient photocurrent response, galvanostatic charge/discharge and electrochemical impedance measurements, it was established that cation-intercalation phenomena were principally responsible for charge-accumulation in the composite and that the incorporation of ionic species into interstitial surface sites was more energetically favourable for protons than for sodium ions. The composite displayed promising capacitive performance in the tested electrolytes, exhibiting Coulombic efficiencies of up to 88% under galvanostatic cycling at 1.0 mA cm⁻² alongside a peak differential capacitance value of 560 mF cm⁻² during the discharge phase. From electrochemical impedance spectroscopy data it was further determined that whilst illumination by white light acted to decrease the series resistance of the photoanode, all other resistive and capacitive components of the impedance characteristics were affected negligibly by the irradiation. In combination, the investigations detailed herein provide an instructive resource for the development of CdS/WO_x composites and the optimisation of electrolytes to improve the performance and chemical stability of such materials. Furthermore, the study serves as a potential foundation from which to advance the concept of integrating the conversion and storage of solar energy into a single dual-functional electrode, in turn facilitating a new generation of photo-supercapacitor devices.

1. Introduction

As the international community endeavours to satisfy its energy demands through sustainable means, solar power has experienced the most rapid growth of all renewable energy technologies but nevertheless continues to adopt a minor role in the overall energy landscape: according to a recent review by British Petroleum[1], whilst the output of photovoltaic panels increased at an average global rate of 24.3% in 2019, solar power accounted for just 2.7% of total electricity consumption during that year. In order to enhance our reliance on solar technologies and other renewable resources, it is necessary that the inherent intermittency of the sustainable energy sector is circumvented by implementing effective energy storage solutions to decouple consumer demand from the instantaneous energy supply. Systems such as hydrogen storage[2-5] (in conjunction with electrolysis[6-8]), compressed air storage[9-11] and batteries[12-14] offer a means of fulfilling this objective, with many researchers working

towards domestic-scale setups that could facilitate decentralised energy generation through the emergence of local smart networks of independent self-producers[15].

One of the critical impediments for energy decentralisation is the prohibitive expense of self-production, with financial incentives often required to ensure that the levelised cost of electricity (LCOE) for a residential solar/battery microgrid is competitive with grid tariffs over the lifespan of the system[16]. In order to improve the durability and efficiency of such a configuration, an electrochemical supercapacitor may be incorporated into the design; these devices are characteristically able to transfer electrical energy at high power densities, thereby supporting transient demand spikes induced by switching loads or sudden variations in the available supply[17]. This hybrid pairing of a battery and a supercapacitor offers a way of enhancing battery longevity by ensuring that battery cycling is used exclusively to accommodate continuous, low-frequency components of the supply and load profiles, decreasing the average depth-of-discharge of the battery during system operation.

As an extension to the concept of a solar-powered microgrid comprising battery and supercapacitor storage, researchers have begun to explore the possibility of augmenting the conversion and storage efficiencies by integrating a supercapacitor into the structure of a photovoltaic cell[18-21]. This device, known as a “photo-supercapacitor” (PS), is most commonly constructed as a monolithic three-electrode arrangement wherein the supercapacitor and solar cell share a common counter electrode located at the centre of the configuration. Controlling circuitry is employed to access the two modules of the device independently of one another, enabling power to be extracted strategically from either the supercapacitor or the solar cell. During photo-charging, the circuit disconnects both modules from the load and allows charge to be transferred from the irradiated photoanode of the photovoltaic section to the working electrode of the supercapacitor. By utilising a plethora of electrode and electrolyte combinations, monolithic three-electrode PS systems[22-26] have been developed that exhibit typical current densities in the range 14-19 mA cm⁻², open-circuit potentials of 0.7-1.0 V, photovoltaic fill factors of between 0.5 and 0.7, and integral capacitance values on the order of 10-100 mF cm⁻² at a galvanostatic discharge current density of at 1.0 mA cm⁻².

However, despite the success of three-electrode PS designs at the laboratory-scale, the segregation of energy conversion and storage within these devices remains conceptually similar to the rudimentary modular approach of implementing supercapacitor storage alongside a separate, standalone solar cell. Indeed, whilst the introduction of a common counter electrode serves to improve storage efficiency by minimising the electrical resistance encountered by charge travelling between the photovoltaic and supercapacitor modules, one cannot significantly reduce the size, complexity or cost of a solar cell/supercapacitor pairing without integrating the two devices in a more meaningful manner. To this end, the present authors recently explored the concept of simultaneously converting and storing energy from solar irradiation at a single photocapacitive working electrode[27], which was achieved through the low-temperature solvothermal synthesis of a cadmium(II) sulphide (CdS)/tungsten(VI) suboxide (WO_x) nanocomposite. By combining X-ray and UV photoelectron spectroscopy (XPS and UPS, respectively) measurements with Tauc plots constructed from diffuse reflectance spectroscopy (DRS) data, it was possible to relate the three-electrode transient photocurrent response (TPR) of the material to the relative valence and conduction band energies of the CdS and WO_x components. In particular, it was surmised that the measurement of a tenfold photocurrent enhancement with respect to a CdS electrode may be rationalised as a Z-scheme

of electron exchange[28] between the conduction band of the semi-metallic WO_x to the valence band of CdS. It was further suggested that the capacitive behaviour of the composite resulted from the trapping of photoexcited valence electrons at the WO_x surface.

In the present work, three-electrode electrochemical investigations are employed to identify the underlying pseudocapacitance mechanisms of the CdS/ WO_x nanocomposite in acidic aqueous electrolytes. By measuring the equivalent series resistance (ESR) and the differential capacitance at different galvanostatic charge/discharge currents in various solutions of acetic acid and sodium acetate, the effects of proton- and sodium-intercalation[29-31] are explored in relation to the measured pseudocapacitance. Moreover, the solar conversion efficiency and chemical stability of the composite under cycled irradiation are assessed for each electrolyte system, providing qualitative insight into the impacts of different ionic species on essential aspects of photoanode performance.

2. Experimental Methods

2.1. Composite synthesis

The CdS/ WO_x nanocomposite was synthesised in accordance with a two-step solvothermal protocol reported previously by the present authors[27]. In the first phase of this process, CdS nanoparticles were produced by heating a 60 mL aqueous solution of cadmium(II) acetate (167 mM) and thiourea (333 mM) at 180 °C for ten hours inside a 125 mL stainless steel Parr acid digestion bomb. After allowing the vessel to cool naturally to room temperature, the CdS product was cleaned through repeated centrifugation into deionised water and absolute ethanol, before being dried overnight at 80 °C. Finally, the CdS was ground into a fine powder using a pestle and mortar.

In the second synthesis step, oxygen-deficient WO_x nanowires were grown solvothermally at the surface of the CdS nanoparticles. Following approximately eight minutes of sonication in absolute ethanol (10 mL), the CdS (20 mM) was added to a 60 mL solution of tungsten(VI) chloride (20 mM) in a 4:1 v/v mixture of absolute ethanol and ethylene glycol, with the resulting suspension then sealed inside a 125 mL stainless steel Parr acid digestion bomb and heated at 180 °C for a period of 24 hours. The bomb was again allowed to cool naturally to room temperature, and the CdS/ WO_x product was subsequently obtained through repeated centrifugation into deionised water and ethanol and drying at 80 °C overnight.

2.2. Electrochemical testing

CdS/ WO_x photoanodes were prepared by firstly sonicating the as-prepared CdS/ WO_x product (5.0 mg) in 1.0 mL of absolute ethanol for a period of twenty minutes, before depositing the suspension dropwise via dropping pipette over a polyimide tape-masked 1.0 cm^2 area of FTO-coated glass (Solaronix TCO22-LI, of quoted resistivity $7 \Omega \text{ sq}^{-1}$) heated at 70 °C on a hot-plate. Following removal of the polyimide mask, exposed areas of the FTO surface were coated with a UV-curing epoxy before exposing the electrode to UV irradiation from a Thermo-Scientific Pierce 8 W UV Lamp (wavelength 302 nm and power

density 2.8 mW cm^{-2}) for one hour. The photoanode was completed by affixing a silver-plated copper wire to the upper end of the electrode using adhesive copper tape.

Electrochemical investigations were conducted through use of a three-electrode setup comprising a Ag/AgCl reference electrode (3M KCl) and platinum-mesh counter electrode, with electronic control and data-acquisition carried out by an Ivium-n-Stat Multichannel Electrochemical Analyser. Three different electrolyte solutions were employed within the study, including solutions of acetic acid (1.0 M, with a measured pH values of 2.2) and aqueous sodium acetate acidified with glacial acetic acid (0.1 M and 6.0 mM, with pH adjustment to a value of 5.0); the pH of each electrolyte solution was measured using a Mettler Toledo FiveGo F2 pH meter, for which pH calibration was achieved through use of phosphate buffer solutions with pH values of 1.68, 7.00 and 10.06. To enable measurement of the transient photocurrent response (TPR) at 0 V *vs* Ag/AgCl, the three-electrode arrangement was placed inside a custom-built LED light-box designed to provide back-illumination of the photoanode at an incident irradiative power density of 100 mW cm^{-2} ; details pertaining to this power density calibration are provided in Fig. S1 of the Supporting Information and the accompanying discussion.

To determine the equivalent series resistance (ESR) and the variation of differential capacitance variation with respect to current density and working potential, galvanostatic charge/discharge experiments were conducted in the dark. In each GCD test, current was allowed to stabilise for one minute at an applied potential of 0.5 V *vs* Ag/AgCl before decreasing the potential at constant current density to a value of either -0.5 V or -1.0 V *vs* Ag/AgCl, depending on the properties of the electrolyte under test. Upon reaching the assigned potential limit, the current was reversed without change to its magnitude in order to ramp the potential of the working electrode back to the starting value of 0.5 V *vs* Ag/AgCl. Values of current density were address in a staggered order for the purpose of identifying any systematic drift during the course of the investigations. In order to eliminate the effects of measurement fluctuations from differential capacitance calculations, a moving average was applied to GCD potential measurements when estimating the time derivative of potential at each data-point; the number of points included in the moving average was selected according to the particular signal-to-noise ratio of a given data-set.

Further evaluation of the impedance characteristics was achieved both by varying the frequency of sinusoidal potential perturbations about a constant direct-current potential bias and by altering the applied potential at a constant perturbation frequency. In the first instance, measurements of the real and imaginary components of impedance were recorded at five frequency values per decade between 15.9 kHz to 0.1 Hz at -0.5 V *vs* Ag/AgCl, using a perturbation amplitude of 10.0 mV and an acquisition time of 10 s at each frequency value; these electrochemical impedance spectroscopy (EIS) experiments were conducted both in darkness and under continuous white light irradiation at a power density of 100 mW cm^{-2} . Mott-Schottky analysis was facilitated by measuring the differential capacitance of each electrode in darkness at working potential intervals of 50 mV between 0.5 V and -1.0 V *vs* Ag/AgCl, with the frequency and amplitude of potential variations set to 1.0 kHz and 10.0 mV, respectively.

3. Results and Discussion

3.1. Transient photocurrent response (TPR)

By investigating the transient photocurrent response (TPR) of the CdS/WO_x nanocomposite in the presence of aqueous sodium sulphate (0.5 M), it was demonstrated in a previous publication by the present authors[27] that the addition of WO_x could be exploited to increase photocurrent under one Sun irradiation by an order of magnitude relative to CdS alone. However, significant electrode instability was evident during the course of these experiments, with the photocurrent halving over a period of approximately twenty minutes from the onset of illumination. Since the equivalent testing of a CdS photoanode yielded a far lower rate of photocurrent decay, it was deduced that degradation of the WO_x component was responsible for the diminishing performance of the photoanode; indeed, it has been shown elsewhere that WO_x compounds are susceptible to attack by peroxy radicals produced during the incomplete oxidation of water molecules[32-34]. Consequently, a key consideration in the design of the present study was the interplay between anionic species and the composite surface, and in particular the capacity of the selected electrolyte to suppress the formation of deleterious peroxy radicals.

In a study by Hill *et al.*[34], the stability of WO₃ electrodes was explored in the presence of sulphate, chloride, phosphate, perchlorate and acetate anions. The investigations revealed that of all of the electrolytes employed, the greatest chemical stability was afforded by acetate ions at a pH value of 3 in the absence of sodium cations. In an attempt to reproduce a similar degree of stability for the present treatment, it was thus decided that the CdS/WO_x photoanodes would be tested in a selection of three aqueous acetic acid and acidified sodium acetate electrolytes; for the purposes of succinctness and ease of reference, the four samples are to be henceforth assigned identifiers of the form “species-concentration-pH”, where the concentration is given in mM and the “species” denominations “NaAc” and “HAc” denote aqueous solutions of sodium acetate (with pH adjustment by glacial acetic acid) and acetic acid, respectively. Four CdS/WO_x photoanodes were prepared, with each allocated one of the three selected electrolytes for electrochemical testing: two photoanodes were tested exclusively in aqueous sodium acetate (0.1 M, with pH adjustment to 5.0), whilst the remaining two electrodes were immersed in an alternative sodium acetate solution (6.0 mM, with pH adjustment to 5.0) or acetic acid (1.0 M, with a measured pH value of 2.2).

It should be recognised that since acetic acid is a weak acid, the concentrations of dissociated hydroxonium cations and acetate anions in the HAc-1000-2.2 solution were 6.0 mM, which is significantly lower than the initial concentration of acetic acid that was introduced into the system. The concentration of sodium acetate in NaAc-6-5.0 was deliberately matched to the acetate anion concentration in HAc-1000-2.2 in order to enable the individual effects of the sodium and hydroxonium cations to be discerned from electrochemical measurements. In the case of the NaAc-100-5.0 systems, the testing of two equivalent electrodes in the same sodium acetate electrolyte was designed to evaluate the impacts of repeatability issues such as differences in surface-coverage or inhomogeneities within the CdS/WO_x stock powder; in order to distinguish between these systems in the

upcoming discussions, the NaAc-100-5.0 identifier is to be appended with the suffix “a” or “b” as required.

In the first phase of the electrochemical investigations, each of the four CdS/WO_x photoanodes was exposed to a square-wave pulse-train of white light irradiation at a power density of 100 mW cm⁻², and the resulting photocurrent was measured at an applied working electrode potential of 0 V vs Ag/AgCl. As shown in Fig. 1a, which plots the photocurrent density, J , as a function of time, t , the NaAc-100-5.0 electrodes delivered highly disparate photocurrent behaviours despite the identical experimental conditions of the two systems. Indeed, the photocurrent generated by NaAc-100-5.0b was of lower magnitude than the corresponding current from NaAc-6-5.0, even though the latter contained 94% fewer sodium and acetate ions. Normalisation of the measurements, depicted in Fig. 1b, reveals that the NaAc-100-5.0 systems also exhibited different rates of photocurrent decay, suggesting that the degradation of CdS/WO_x was intrinsically linked to current density and, accordingly, the rate of charge-exchange between the electrolyte and composite. Nevertheless, the deterioration rate of NaAc-100-5.0b was remarkably similar to rate of photocurrent decay in HaAc-100-2.2, which produced by far the largest photocurrent response of the four systems. It is therefore evident that the properties of a TPR signal generated at constant working potential are strongly dependent on indeterminate factors involved in sample preparation, and that these may be sufficient to offset variations resulting from modifications to the electrolyte solution.

From the outlined discrepancies in Fig. 1 it is clear that whilst the TPR measurements offer a qualitative indication of system behaviours, they cannot be used to attain quantitative insight into impedance properties or the mechanisms responsible for the observed photocapacitance characteristics. Furthermore, it is important to acknowledge that the TPR experiments represented in Fig. 1 correspond to a single working electrode potential, and hence they provide no information pertaining to the variation of impedance components with respect to the potential, current density or the frequency of potential perturbations. In order to better understand these relationships, it is necessary to address alternative characterisation techniques including galvanostatic charge/discharge (GCD) testing and electrochemical impedance measurements.

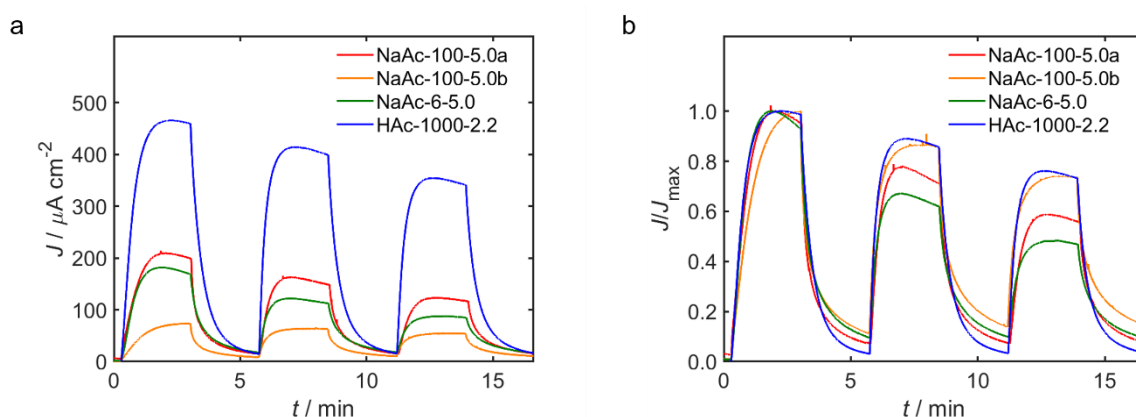


Fig. 1. Absolute (a) and normalised (b) transient photocurrent response (TPR) data from CdS/WO_x photoanodes in various aqueous electrolytes under pulsed white light irradiance at a calibrated incident power density of 100 mW cm⁻².

3.2. Galvanostatic charge/discharge (GCD)

In the direct-current mode of operation, it is commonly appropriate to represent a capacitive electrode as an equivalent circuit composed of a constant “equivalent series resistance” (ESR), R_{ESR} , in series with a differential areal capacitance, C , that accounts for the combination of electric double-layer capacitances and pseudocapacitances associated with charge-exchange mechanisms between the electrode and surrounding electrolyte[31, 35]; the validity of the assumption that R_{ESR} is constant is verified in Section 3.3 through consideration of electrochemical impedance measurements. By invoking Ohm’s law, the measured potential difference V across the electrode during a charging phase follows the first-order differential equation

$$R_{\text{ESR}}C \frac{dJ}{dt} + J - C \frac{dV}{dt} = 0, \quad (1)$$

where J denotes the current density through the electrode and t is the charging time. One may similarly describe the discharge behaviour through use of the expression

$$R_{\text{ESR}}C \frac{dJ}{dt} - J + C \frac{dV}{dt} = 0, \quad (2)$$

where t now corresponds to the total time of discharge. During a complete galvanostatic charge/discharge (GCD) cycle, the magnitude of J is held constant so that the time derivative of J vanishes; accordingly, Eqs. (1) and (2) yield the relation

$$C = \left| J \left(\frac{dV}{dt} \right)^{-1} \right|, \quad (3)$$

which enables the functional form of $C(V)$ to be evaluated from the measured derivative of V with respect to t . Furthermore, since it is necessary to impose the condition that the potential difference across C is continuous at the changeover between the charging and discharging phases, V exhibits a discontinuity of magnitude ΔV_{cd} at this point, where

$$\Delta V_{\text{cd}} = 2JR_{\text{ESR}}. \quad (4)$$

Provided that the series equivalent circuit delivers an adequate approximation of a pseudocapacitive electrode, it is thus possible to derive estimates for both C and R_{ESR} from the GCD characteristics of the system.

GCD measurements obtained from the four CdS/WO_x photoanodes are displayed in Fig. 2; all of the tests were undertaken from a starting working electrode potential of 0.5 V vs Ag/AgCl, with subsequent charging and discharging carried out at a constant current of magnitude J . By recalling the form of Eq. (3) it is evident that NaAc-6-5.0 exhibited a far lower storage capacity than the other three systems over the investigated ranges of J and V , despite the 6.0 mM sodium acetate solution comprising the same concentrations of cations and acetate anions as the 1.0 M acetic acid electrolyte. One may infer from this result that the intercalation of protons into WO_x micropores occurred more readily than the equivalent intercalation of sodium, which is attributable to the larger radius[36] and correspondingly inferior ionic mobility of a sodium cation[37-39], in addition to the relatively high energy cost of detaching its solvation sphere[40]. Nevertheless, the ability of sodium ions to contribute to the overall pseudocapacitance is evidenced by the GCD behaviours of the NaAc-100-5.0 systems, for which the rate of potential change at given J was of similar

magnitude to the equivalent HAc-1000-2.2 data-set. Indeed, since the pH values of NaAc-6-5.0 and NaAc-100-5.0 were identical, it follows that the different sodium concentrations were alone responsible for the disparate capacitances of these systems, and moreover that sodium-intercalation was the predominant pseudocapacitance mechanism in each case.

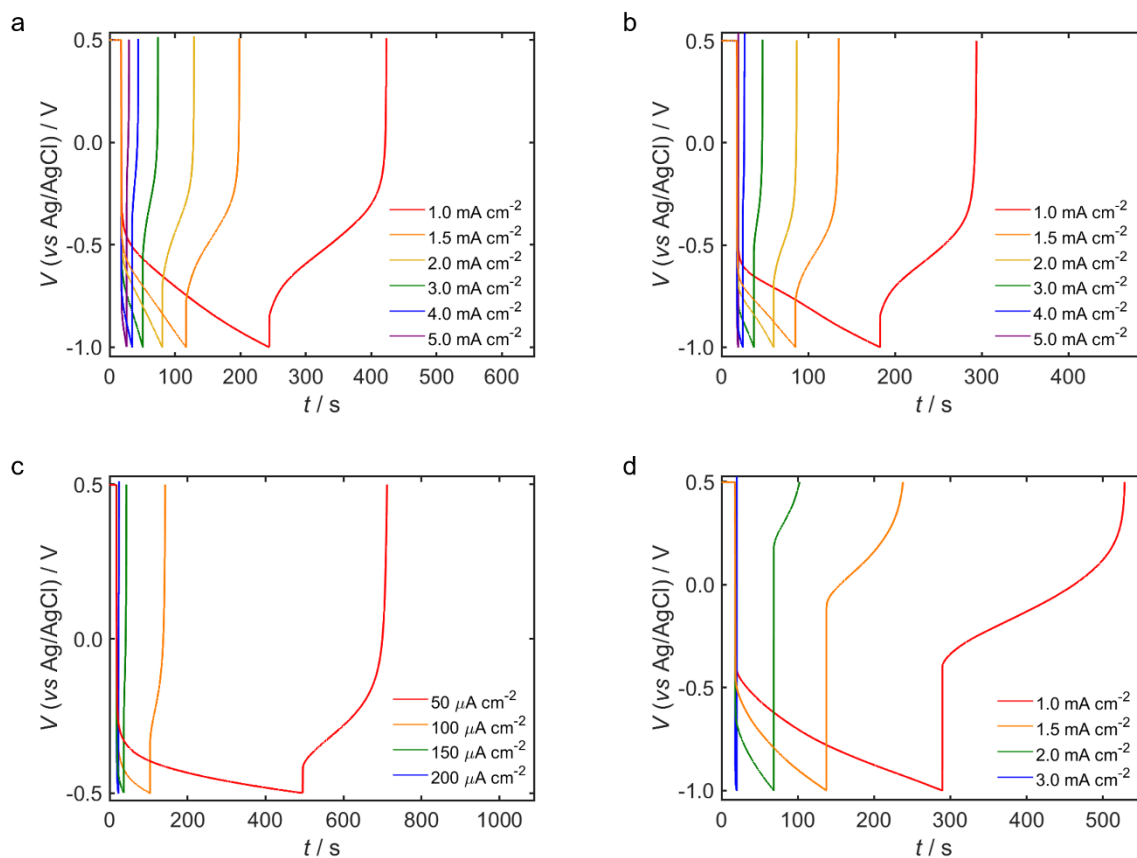


Fig. 2. Galvanostatic charge/discharge (GCD) potential measurements from the NaAc-100-5.0a (a), NaAc-100-5.0b (b), NaAc-6-5.0 (c) and HAc-1000-2.2 (d) systems acquired in the dark at various magnitudes of galvanostatic charge/discharge current density.

In accordance with mean-field capacitance theories such as the Goodwin-Kornyshev model[41-43] and computational treatments that attempt to encompass the effects of intercalation processes[44-46], charge accumulation at the CdS/WO_x exhibited a strong potential dependence and the electrodes possessed negligible capacitance above a particular potential value known as the “potential of zero charge”. A more quantitative comparison of the present pseudocapacitance behaviours is facilitated by Fig. 3, which plots the $C(V)$ functions derived by applying Eq. (3) to the GCD traces shown in Fig. 2; it is worth noting that the C values achieved by the HAc-1000-2.2 and NaAc-100-5.0 electrodes at 1.0 mA cm⁻² are of comparable magnitude to the corresponding integral capacitance estimates for reported photo-supercapacitor prototypes addressed in the Introduction, although one should recognise that the integral capacitance averages the time derivative of V across the entire potential window. Despite the marked disparities between the TPR properties of the two NaAc-100-5.0 systems, the corresponding $C(V)$ relationships shown in Figs. 3a and b are remarkably similar in form, albeit with significant differences in magnitude. Due to the rudimentary nature of the drop-casting deposition protocol used to prepare the composite films, however, it is likely that these differences are attributable to variations in CdS/WO_x

surface coverage between the two NaAc-100-5.0 electrodes. Another discrepancy between NaAc-100-5.0a and NaAc-100-5.0b are the appearance of local maxima in the capacitive charging trends of Fig. 3b that are notably absent from the equivalent measurements in Fig. 3a. Yet despite the seemingly conspicuous nature of these peaks, it is worth noting that they originate from near-imperceptible variations in the gradients of the charging curves depicted in Fig. 2b; for this reason, it is possible that the maxima in Fig. 3b are experimental artefacts rather than manifestations of an underlying physical phenomenon.

In contrast to Figs. 3a and b, the $C(V)$ relationships of NaAc-6-5.0 plotted in Fig. 3c are indicative of charge/discharge cycles with low Coulombic efficiencies, as the cumulative area bounded by each discharge curve is considerably lower than the associated area of the charging phase that precedes it. Conversely, the HAc-1000-2.2 system was ostensibly able to retain a high proportion of incident charge at J values of 1.0-2.0 mA cm^{-2} , as the associated charge and discharge relationships in Fig. 3d enclose areas of comparable magnitude. At higher current densities, however, the Coulombic efficiency diminished due to the large potential offset between the end of the charging phase and the beginning of the subsequent discharge, which, from Eq. (4), is indicative of a high-valued ESR.

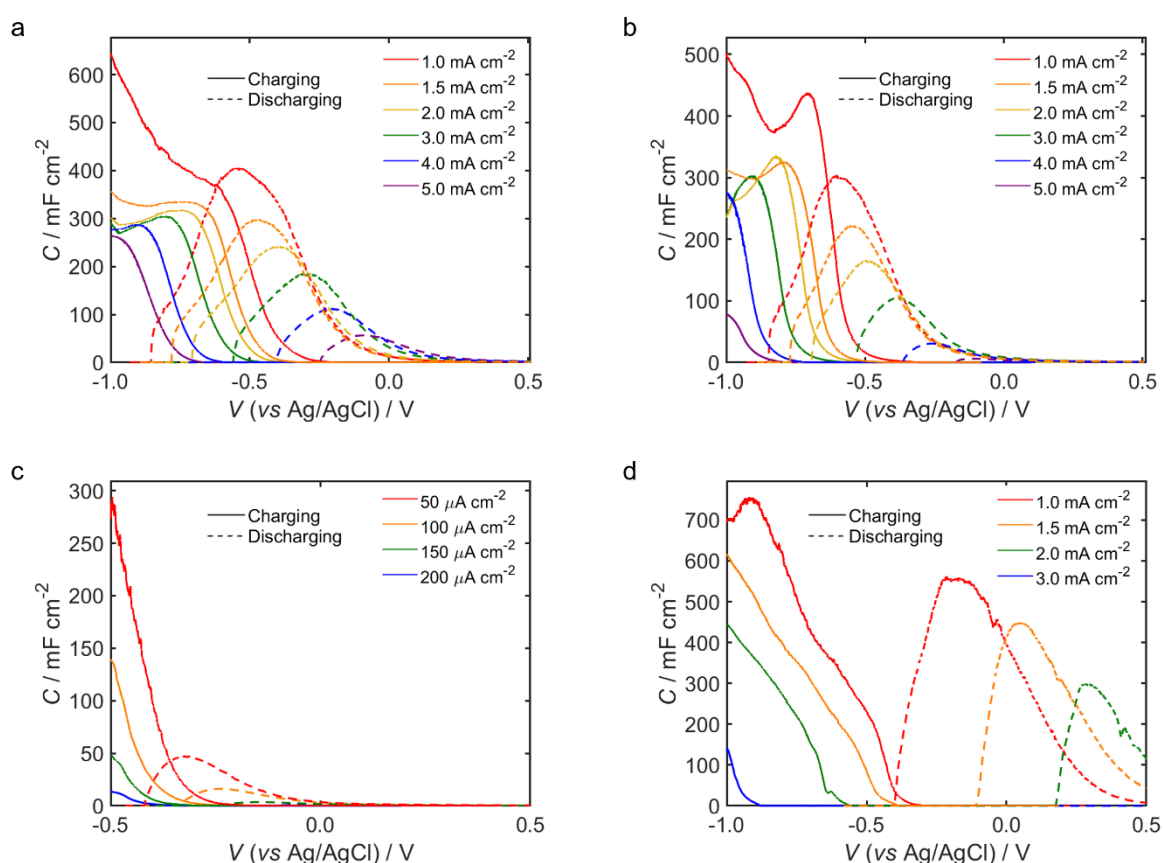


Fig. 3. Calculated relationships between the differential capacitance, C , and potential, V , during the charge/discharge phases of NaAc-100-5.0a (a), NaAc-100-5.0b (b), NaAc-6-5.0 (c) and HAc-1000-2.2 (d) at various galvanostatic current densities; these trends were acquired via application of Eq. (3) to the corresponding galvanostatic charge/discharge (GCD) measurements displayed in Fig. 2.

To explore the effect of the electrolyte on R_{ESR} , Fig. 4 depicts the measured relationships between the potential discontinuity ΔV_{cd} at the charge/discharge changeover and the applied current density. The assumption that the ESR represents a constant series resistance is supported by the plotted trends, as in all instances ΔV_{cd} was found to scale in direct proportion to J , in accordance with Eq. (4). Comparison of the ESRs once again illustrates the electrochemical similarity between the NaAc-100-5.0 systems, with the R_{ESR} estimates obtained from the gradients of Figs. 4a and b differing by approximately 3% from the mean of the two values. Conversely, the calculated ESR of NaAc-6-5.0 was a factor of 2.6 higher than the ESR of HAc-1000-2.2, despite the equal cation and acetate anion concentrations of these systems; it is therefore apparent that the nature of the cationic species had a considerable influence not only on the measured pseudocapacitance of the CdS/WO_x photoanode, but also on the resistance encountered during charge-transfer across the electrode/electrolyte interface. This result reinforces the previous deduction that whilst protons and sodium cations were both able to intercalate into the WO_x surface lattice structure, the intercalation process was either thermodynamically or kinetically more favourable in the latter case.

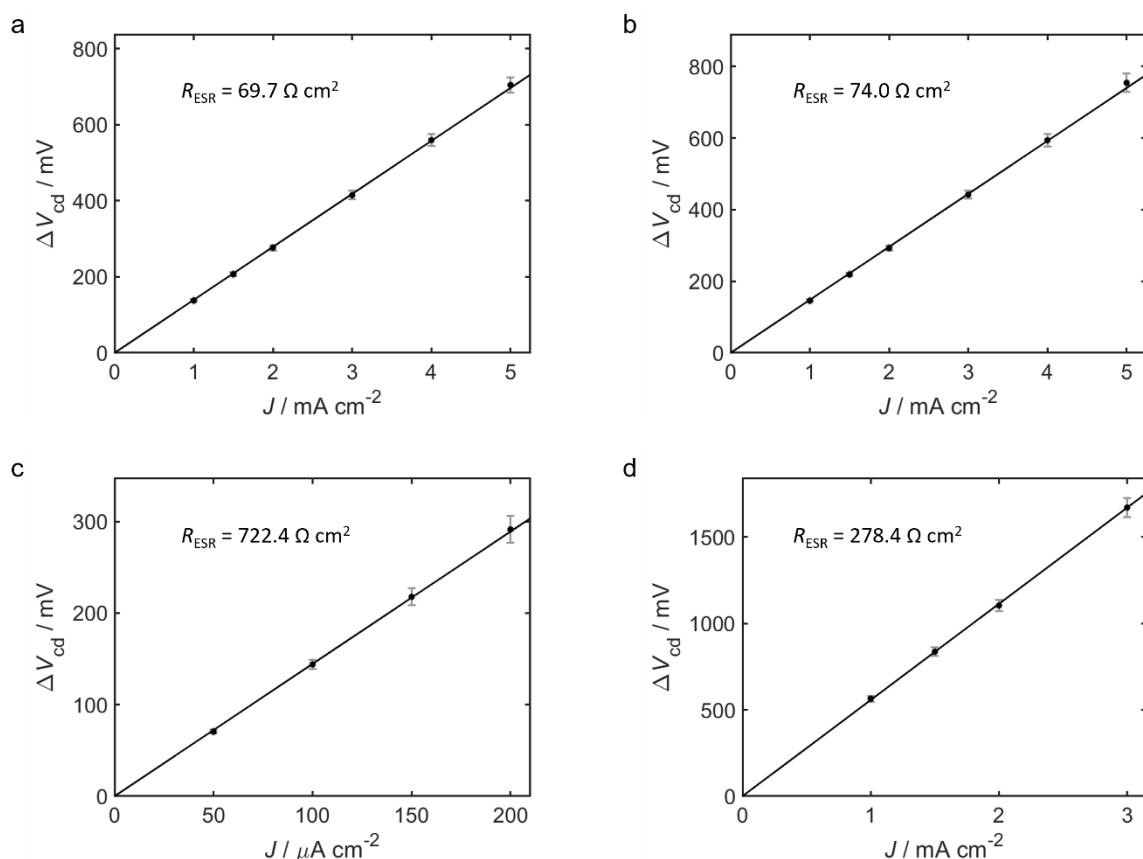


Fig. 4. Estimated variations of the potential discontinuity, ΔV_{cd} , between the galvanostatic charge and discharge phases of NaAc-100-5.0a (a), NaAc-100-5.0b (b), NaAc-6-5.0 (c) and HAc-1000-2.2 as a function of the current density J ; each ΔV_{cd} value was acquired by consulting the relevant galvanostatic charge/discharge (GCD) data-set shown in Fig. 2, and the equivalent series resistance (ESR), R_{ESR} , of the systems were determined by inserting the measured gradients of the linear $\Delta V_{\text{cd}}(J)$ relationships into Eq. (4).

It was noted previously that the Coulombic efficiency, η_Q , of an electrode is intrinsically linked to the ESR of the system, with a high ESR reducing the range of J values over which high Coulombic efficiency can be sustained. This point is further illustrated by explicitly evaluating the Coulombic efficiency according to the definition[47]

$$\eta_Q = 100 \frac{Q_d}{Q_c} \%, \quad (5)$$

where Q_c and Q_d respectively denote the total charge transferred during a charging or discharging phase. The quantities may be calculated either by integrating $C(V)$ with respect to V over the entire potential range or by taking the product of J and the duration of the charging/discharging phase; in the present analysis, η_Q has been approximated as the mean of the two values generated by these alternative methods, with the assumed uncertainty in the resulting estimate given as the difference between each value and the mean. As shown in Fig. 5, the Coulombic efficiency of all four systems declined with increasing J , with NaAc-6-5.0 producing η_Q values of less than 50% despite the low current densities employed during GCD testing of the system. Whilst the η_Q values of NaAc-100-5.0 and HAC-1000-2.2 remained above 60% when J was less than or equal to 2 mA cm⁻², the Coulombic efficiency of the latter system decreased to approximately 1% at 3 mA cm⁻²; as acknowledged previously, the superior efficiencies of the NaAc-100-5.0 systems at high current densities correlates with the relatively low R_{ESR} value of the 100 mM sodium acetate electrolyte.

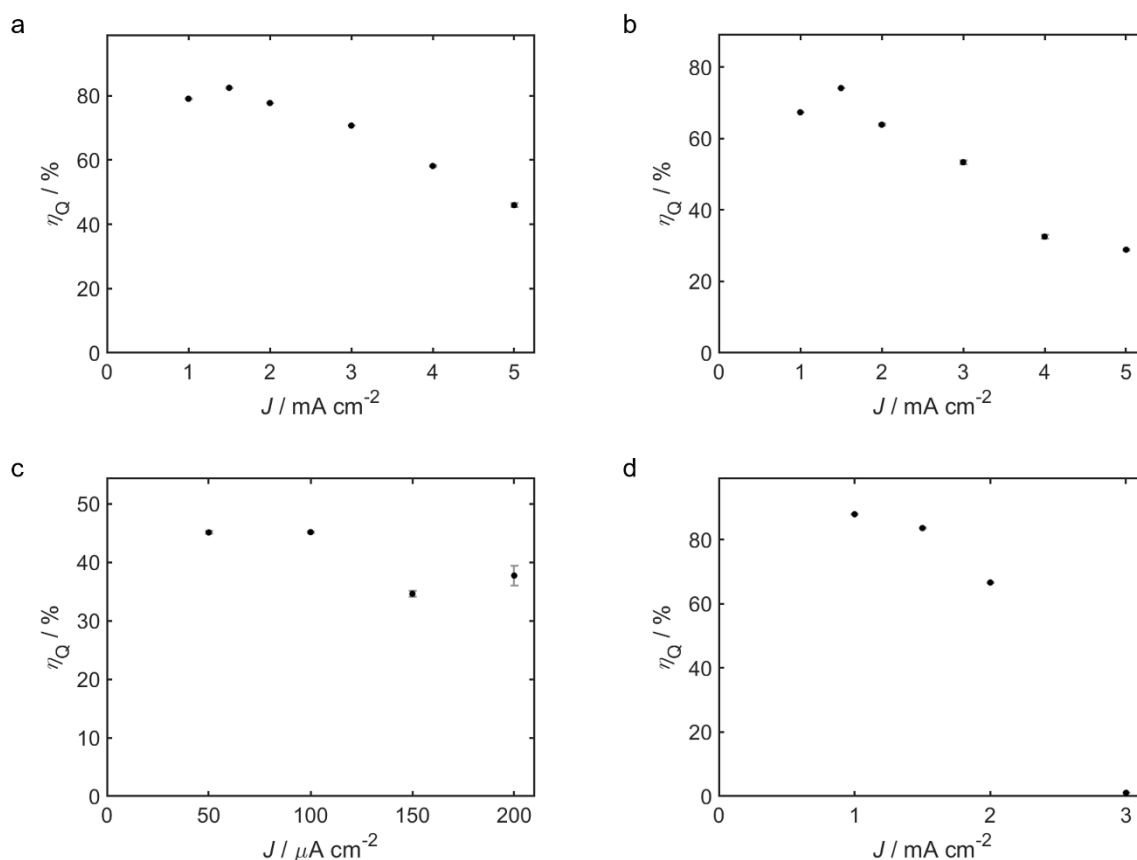


Fig. 5. Coulombic efficiency, η_Q , of galvanostatic charge/discharge (GCD) cycles as a function of current density J in the case of NaAc-100-5.0a (a), NaAc-100-5.0b, NaAc-6-5.0 (c) and HAC-1000-2.2 (d). Estimates of η_Q were obtained by applying Eq. (5) to the

GCD measurements depicted in Fig. 2, with the total charge exchanged during a charge/discharge phase equated to either the product of J and the phase duration or the area enclosed by the relationship between differential capacitance, C , and potential, V ; the plotted η_Q data are given by the mean of the η_Q values yielded by these methods, with the uncertainty in each η_Q data-point approximated as half of the difference between the two η_Q estimates.

3.3. Electrochemical impedance measurements

Whilst GCD testing enables the analysis of the direct-current resistance and capacitance properties of an electrochemical system, one must utilise electrochemical impedance techniques to assess how these variables behave with respect to the magnitude or oscillation frequency, f , of the applied potential. An oft-used method for characterising the $C(V)$ variation at a single kHz-scale frequency of sinusoidal potential perturbations is Mott-Schottky analysis, which affords insight into the energy level structure of an electrode material[48]. Provided that the Mott-Schottky experiment is conducted at a sufficiently value of f , the period of the oscillations is too short for charge-exchange processes to contribute significantly to the overall capacitance of the system[49]. Consequently, the predominant capacitance mechanism is the formation of a surface space-charge region that is charge-balanced by the interfacial accumulation of electrolytic species within a region known as the Helmholtz layer; this phenomenon manifests as an electric double-layer capacitance, C_{dl} , that is typically several orders of magnitude smaller than the pseudocapacitance at zero frequency. If one assumes that the capacitance of the Helmholtz layer, C_H , is much greater than the space-charge capacitance at the electrode surface, the inverse square of the measured capacitance can be expressed as[48]

$$C_{dl}^{-2} = \frac{2}{\varepsilon_0 \varepsilon q N_D} \left(V - V_{FB} - \frac{k_B T}{q} \right), \quad (6)$$

where ε_0 and ε respectively denote the permittivity of free-space and the relative permittivity of the electrode material, k_B is Boltzmann's constant, T is temperature, q is the elementary unit of electronic charge, N_D is the volume density of surface donor states and V_{FB} is the "flat-band potential" of the electrode, which is defined as the value of V at which there is zero band-bending at the electrode surface. By invoking Eq. (6) in conjunction with prior knowledge of ε , it is possible to approximate N_D from the gradient in the linear regime of the measured $C_{dl}(V)^{-2}$ function, whilst extrapolation of this linear relationship to infinite C_{dl} enables estimation of V_{FB} .

In Fig. 6, Mott-Schottky plots have been constructed from C_{dl} measurements corresponding to the NaAc-100-5.0 and HAc-1000-2.2 systems at a constant potential perturbation frequency of 1.0 kHz; the C_{dl} range spanned by NaAc-6-5.0 was significantly lower than in the three systems represented in Fig. 6a, so, for the purpose of visual clarity, this electrode is addressed separately in Fig. 6b. A linear fitting function (plotted as a dashed grey line) has been generated for each data-set by applying a least-squares regression protocol to data-points for which the gradient of $C_{dl}(V)^{-2}$ is greater than two thirds of the maximum value. The functional form of the $C_{dl}(V)^{-2}$ relationship varies little between the two NaAc-100-5.0 data-sets, and the consistency between the corresponding linear fits indicates that these systems possessed similar concentrations of surface donor states. Although there is a notable offset between the NaAc-100-5.0 traces, yielding a

difference of approximately 77 mV between the associated V_{FB} estimates, this discrepancy is possibly attributable to a marginal difference in the Helmholtz capacitances of the two samples, as evidenced by the disparate plateau values of C_{dl} when V is significantly more negative than V_{FB} [50, 51]; indeed, in cases where C_{H} is insufficiently large for its series contribution to C_{dl} to be disregarded, $C_{\text{dl}}(V)^{-2}$ deviates from the form predicted by Eq. (6) and one can no longer reliably estimate N_{D} or V_{FB} from the gradient and x-intercept, respectively, of the Mott-Schottky plot. As in the case of the $C(V)$ trends from Figs. 3a and b, it is possible that such variations in the constituent components of C_{dl} are indicative of differences between the areal coverages of the NaAc-100-5.0 electrodes.

The final relationship depicted in Fig. 6a belongs to HAc-1000-2.2, and it is characterised by a sharp change in C_{dl} that produces a V_{FB} estimate in the vicinity of 0 V vs Ag/AgCl. Whilst formal estimation of N_{D} from the linear regime of $C_{\text{dl}}(V)^{-2}$ is problematic due to aforementioned considerations regarding the relative magnitudes of the Helmholtz and space-charge capacitance contributions, it is nevertheless instructive to apply Eq. (6) as a means of identifying qualitative differences between electrode surface characteristics. Approximating ϵ as 50, which is typical value for WO_x films[33], and further assuming a standard system temperature of 298.15 K, an N_{D} value of $3.26 \times 10^{19} \text{ cm}^{-3}$ is obtained for the HAc-1000-2.2 system; this N_{D} estimate is significantly lower than corresponding figures of $1.21 \times 10^{20} \text{ cm}^{-3}$ and $1.55 \times 10^{20} \text{ cm}^{-3}$ acquired from the NaAc-100-5.0 fits under the same assumptions. This marked difference between the NaAc-100-5.0 and HAc-1000-2.2 systems indicates that electronic surface properties of the CdS/ WO_x composite were modified by chemical interactions with the electrolyte.

It is evident from the Mott-Schottky analysis of NaAc-6-5.0 and HAc-1000-2.2 that hydroxonium ions supported a higher quantity of electrode surface charge than an equivalent concentration of sodium ions, as the former system exhibited markedly lower C values at a given bias potential; this result is possibly attributable to the relatively low diameter of hydroxonium ions with respect to their sodium counterparts, yielding a greater charge density an enhanced capacity to access surface sites. The Mott-Schottky plots in Fig. 6 may also be used to quantify the relative impacts on the cation species on donor density: the linear portion of the NaAc-6-5.0 data-set yields a value of 4.39×10^{19} for N_{D} , which is marginally higher than the corresponding N_{D} estimate of HAc-1000-2.2. However, one should again recall that the reliability of each N_{D} estimate is contingent on the Helmholtz layer exhibiting a much greater capacitance than the space-charge region; this condition is not adequately satisfied by the NaAc-6-5.0 and HAc-1000-2.2 data-sets, as the magnitude of C^{-2} did not become negligible as the bias potential tended towards increasingly negative values. It is also important to recognise that the high ESR of NaAc-6-5.0 significantly suppressed current density during impedance measurements, which in turn introduced sizeable uncertainties into the Mott-Schottky plot displayed in Fig. 6b. For these reasons, one cannot reasonably infer phenomenological differences in the interactions of hydroxonium and sodium ions with surface donor states from the disparity between the N_{D} estimates of NaAc-6-5.0 and HAc-1000-2.2.

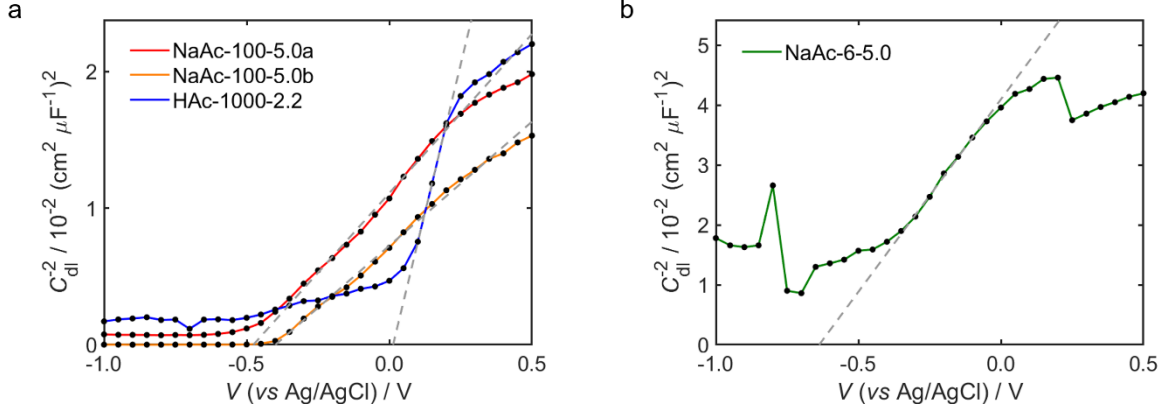


Fig. 6. Mott-Schottky plots relating the electric double-layer capacitance, C_{dl} , of the HAc-1000-2.2 and NaAc-100-5.0 systems (a) or NaAc-6-5.0 (b) to the potential applied to the unirradiated CdS/WO_x electrode at a constant potential perturbation frequency of 1.0 kHz; within each data-set, a linear fit (depicted as a dashed line) has been applied to data-points that correspond to a gradient with magnitude greater than two-thirds of the maximum value. In accordance with Eq. (6), the donor state density, N_D , and flat-band potential, V_{FB} , of a given system are estimable from the gradient and x-intercept, respectively, of the linear fit, provided that the capacitance of the Helmholtz layer, C_H , was much greater than the corresponding capacitance of the space-charge region.

Mott-Schottky and GCD analyses share the common feature of characterising the capacitance of an electrode at a single frequency of potential perturbations. In order to investigate the variation of capacitance as a function of f one must instead utilise electrochemical impedance spectroscopy (EIS), wherein the real and imaginary components of system impedance, Z , are determined over a range of oscillation frequencies at a constant bias potential. From these measurements it is possible to quantify various aspects of the electrochemical system in terms of the elements of an appropriate equivalent circuit model such as the example illustrated in Fig. 7[52-55]; for instance, the extrapolated resistance in the limit of infinite f corresponds to the total series resistance of the electrode and electrolyte combination, R_{in} , whilst the electric double-layer capacitance, C_{dl} , and the effective resistance of charge-transfer processes, R_{ct} , are commonly estimable from the diameter and peak position of the semi-circular relationship between imaginary and real impedance at intermediate frequencies. As one approaches the direct-current mode of operation, the EIS behaviour is predominantly dictated by pseudocapacitance mechanisms; this contribution can often be described by a finite-space Warburg impedance, Z_W , given by[53-61]

$$Z_W = \sqrt{\frac{3R_D}{i\omega C_D}} \coth(\sqrt{3i\omega R_D C_D}), \quad (7)$$

where ω is the angular frequency of potential oscillations, and R_D and C_D respectively correspond to characteristic resistance and capacitance values from an open-circuit transmission-line model of species diffusion. One should acknowledge that in the limit of zero f , whereupon Eq. (7) simplifies to

$$\lim_{\omega \rightarrow 0} Z_W = R_D + \frac{1}{i\omega C_D} \quad (8)$$

and Z can be correspondingly expressed as

$$\lim_{\omega \rightarrow 0} Z = R_{in} + \frac{(R_{ct} + R_D)C_D^2}{(C_{dl} + C_D)^2} + \frac{1}{i\omega(C_{dl} + C_D)}, \quad (9)$$

it follows from the schematic in Fig. 7 that if C_D is much greater than C_{dl} , the C and R_{ESR} estimates yielded by GCD analysis are equivalent to C_D and the sum of R_{in} , R_{ct} and R_D , respectively.

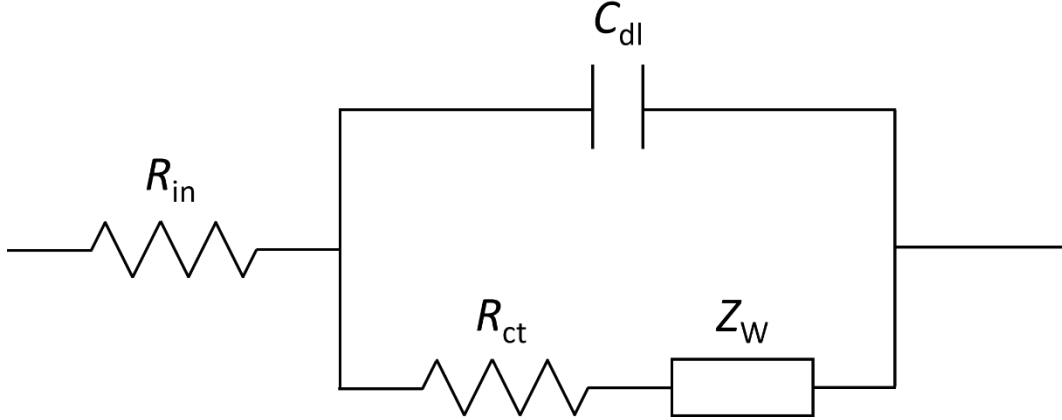


Fig. 7. Schematic representation of an equivalent circuit commonly used to describe the impedance characteristics of a pseudocapacitive supercapacitor system. The circuit comprises an electric double-layer capacitance, C_{dl} , a series resistance, R_{in} , that corresponds to the system resistance in the limit of infinite frequency, a second resistance, R_{ct} , associated with energy losses during charge-transfer processes between the electrode and electrolyte, and a finite-space Warburg impedance, Z_W , generated by intercalation phenomena.

By making use of the EIS technique, it is possible to explore how different stimuli influence the impedance behaviour of an electrochemical system. To this end, Fig. 8 depicts the effects of irradiance and applied bias potential on the impedance spectra of NaAc-100-5.0a, with the results provided in the form of a logarithmic Bode plot in Fig. 8a and as a Nyquist plot in Fig. 8b. By holding the bias potential of the photoanode constant with respect to the Ag/AgCl reference electrode throughout each EIS test, incident white light could not alter the quasi-Fermi level of electrons within the CdS/ WO_x composite, meaning that the equilibrium concentration of conduction band electrons could not be varied by the irradiance. For this reason, any discrepancies between the “light” and “dark” impedance relationships at a given bias potential must be ascribed to light-induced alterations to the intrinsic resistances or capacitances of the electrochemical system. Conversely, the “dark” data-sets represented in Fig. 8 were acquired under identical conditions except for the bias potential applied in each case, with the potential difference between experiments corresponding to a proportional shift in the quasi-Fermi level of electrons and a resulting variation in the population of conduction band states.

It is evident from both representations of the EIS data that irradiation of the photoanode at constant working potential had a negligible influence on impedance characteristics at frequencies exceeding 100 Hz, although a minor deviation occurred at lower frequencies. In the latter instance, the derivative of $\text{Im}(Z)$ with respect to $\text{Re}(Z)$ was ostensibly unaffected by white light illumination, suggesting that resistance contributions were alone

responsible for the measured change in Z . By contrast, a negative shift of the working potential produced a systematic, frequency-invariant decrease in Z ; this phenomenon is consistent with a reduction in the value of R_{in} , leading to a translation of the Nyquist plot along the real axis without altering its form. Recalling the derivation of Eq. (4) in Section 3.2, one should note that this potential-dependence of R_{in} contradicts the previous assumption that R_{ESR} remained constant as a function of applied potential; however, the variation in R_{in} between -0.5 V and -1.0 V vs Ag/AgCl represents a small percentage of the measured ESR, and hence the assumed potential-invariance of R_{ESR} is approximately satisfied over the experimental potential range.

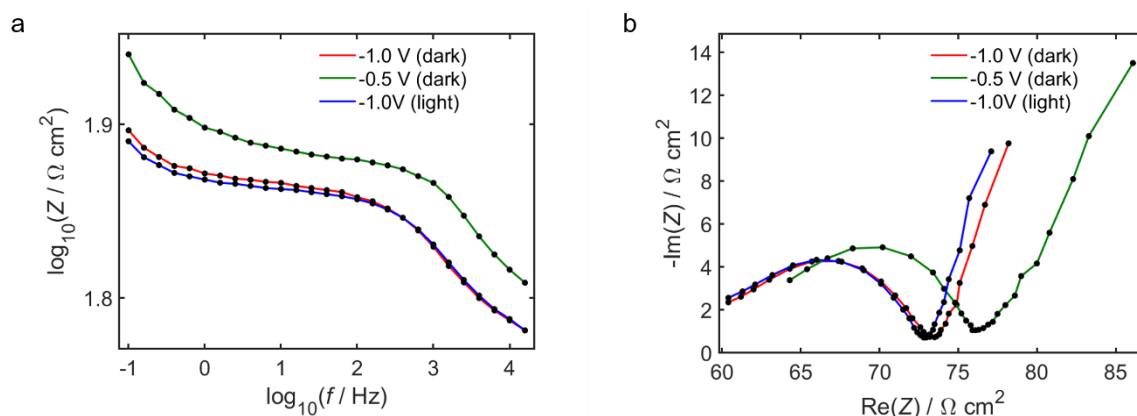


Fig. 8. Bode (a) and Nyquist (b) plots characterising the relationships between the magnitude of impedance, Z , its real and imaginary components, and the frequency, f , of sinusoidal potential perturbations, measured by electrochemical impedance spectroscopy (EIS); the plotted variations depict NaAc-100-5.0a system behaviours at bias potentials of -1.0 V or -0.5 V vs Ag/AgCl, both in darkness and under irradiance by white light at a calibrated incident power density of 100 mW cm^{-2} .

In combination with the Mott-Schottky analysis and the GCD measurements detailed in Section 3.2, the EIS characterisation of NaAc-100-5.0a provides an instructive illustration of the relationships between externally applied stimuli and various photoelectrochemical properties of CdS/ WO_x . In particular, the outlined comparison of EIS behaviours suggests that whilst a selection of equivalent circuit elements are required to describe the measured impedance behaviours, these components may be regarded as approximately independent of irradiance levels or bias potential, with the exception of the series resistance R_{in} . In a previous publication by the present authors[27] it was demonstrated that the open-circuit potential of CdS/ WO_x becomes increasingly negative when exposed to white light, and hence it follows from the EIS analysis that this incident irradiation can be approximately described as a conventional source of voltage and current in series with the equivalent circuit shown in Fig. 7. This simplified representation of the photoanode serves as a useful means of predicting system performance across a range of load conditions relating to a variety of device applications.

4. Conclusions

By utilising transient photocurrent response (TPR), galvanostatic charge/discharge (GCD), Mott-Schottky and electrochemical impedance spectroscopy (EIS) techniques, the

electrochemical characteristics of a CdS/WO_x nanocomposite have been investigated with the aim of elucidating the underlying charge-storage mechanisms in acidic aqueous electrolytes. Insight into the relative impacts of sodium- and proton-intercalation has been attained through comparison of the capacitance behaviours of CdS/WO_x photoanodes in different acetic acid and acidified sodium acetate electrolytes, with the effects of bias potential, white light irradiance and the frequency of potential perturbations explored during the course of the study.

From GCD testing it was discovered that whilst sodium-intercalation yields a significant contribution to the overall pseudocapacitance of a CdS/WO_x electrode, this process is far less prevalent than proton-intercalation at a given concentration of the intercalating cationic species. In particular it was shown that whilst peak areal capacitance values on the order of 100 mF cm⁻² were attainable during galvanostatic charging at 1.0-3.0 mA cm⁻² in an acetic acid solution containing 6.0 mM hydroxonium ions, areal capacitances of this magnitude could only be achieved by limiting the current density to 200 μA cm⁻² when the hydroxonium content was substituted for an equal concentration of sodium ions. Furthermore, the Coulombic efficiency of a GCD cycle was below 50% at 200 μA cm⁻² in 6.0 mM sodium acetate solution, whereas a corresponding efficiency of more than 80% at 1.0 mA cm⁻² was produced in the case of an acetic acid electrolyte of identical cation concentration. In each of these systems, the low availability of ionic species yielded a high equivalent series resistance that in turn led to a rapid decline in Coulombic efficiency with increasing current density; however, this deterioration was suppressed by augmenting the solution concentration, with the Coulombic efficiency remaining above 50% at 3.0 mA cm⁻² for electrodes immersed in a 100 mM solution of sodium acetate.

In addition to evaluating the dependence of pseudocapacitance on the nature and concentration of the electrolyte, other components of the impedance behaviour were investigated such as the constituent resistances of the system and the electric double-layer capacitance. Through Mott-Schottky analysis of the capacitance as a function of bias potential, it was possible to obtain a quantitative understanding of the relationship between the electrolyte and electronic surface donor states: it was evident, for instance, that electrolytic species acted to modify the density of these states, as a 100 mM sodium acetate solution generated an almost fourfold increase in the estimated donor density relative to an acetic acid electrolyte of lower ion concentration. Furthermore, the relationship between capacitance and bias potential varied considerably upon changing the identity of cation species: sodium ions produced a lower relative permittivity at given bias potential than an equivalent concentration of hydroxonium ions, conceivably due to the higher charge density of the hydroxonium ion and its increased capacity to access surface sites.

Finally, the variation of impedance as a function of potential oscillation frequency was investigated, including the effects of white light irradiance and potential bias. It was demonstrated that whilst a shift in the applied potential resulted in a corresponding decrease in the equivalent series resistance in the infinite frequency limit, incident white light had little effect on the impedance characteristics aside from producing a fractional decrease in the resistance associated with intercalation processes. Neither this resistance nor the equivalent capacitances of the system were appreciably affected by exposure to white light or changes in the applied bias; hence it was suggested that the effects of irradiation may be satisfactorily modelled as a conventional source of voltage and current at the input of the

electrochemical equivalent circuit, with the caveat that the infinite-frequency series resistance exhibits a small but significant dependence on the supplied potential.

The mechanistic insights provided by the present study offer a useful foundation for the future integration of CdS/WO_x composites into functional photo-supercapacitor prototypes. Moreover, whilst it was clear from photocurrent degradation encountered during TPR tests that the chemical stability of the composite in aqueous electrolytes has yet to be resolved, the task of optimising the electrolyte to maximise system performance is facilitated by the discussions outlined herein. Building on the present work, there is considerable scope for further investigations to address residual stability issues and to improve photocurrent density by exploiting alternative deposition techniques and by exploring additional processing steps such as post-annealing of the nanocomposite film. With these improvements, the concept of integrating solar energy conversion and storage into a single dual-functional electrode offers a potentially invaluable route towards enhancing the performance and versatility of photo-supercapacitor devices.

Author Contributions

Daniel Raymond Jones: Conceptualisation, Methodology, Software, Validation, Formal analysis, Investigation, Data curation, Writing – Original draft preparation, Visualisation, Project administration; Charles William Dunnill: Funding acquisition.

Acknowledgements

Financial support was provided by the Welsh Government Sêr Cymru Programme and the Flexis project, which is part-funded by the European Regional Development Fund (ERDF) through the Welsh Government.

Additional Information

The authors declare no competing interests.

References

- [1] Statistical Review of World Energy. 69 ed.: British Petroleum; 2020.
- [2] Barthelemy H, Weber M, Barbier F. Hydrogen storage: Recent improvements and industrial perspectives. *Int J Hydrogen Energ* 2017;42:7254-62.
- [3] Abe JO, Popoola API, Ajenifuja E, Popoola OM. Hydrogen energy, economy and storage: Review and recommendation. *Int J Hydrogen Energ* 2019;44:15072-86.
- [4] Moradi R, Groth KM. Hydrogen storage and delivery: Review of the state of the art technologies and risk and reliability analysis. *Int J Hydrogen Energ* 2019;44:12254-69.
- [5] Ren J, Musyoka NM, Langmi HW, Mathe M, Liao S. Current research trends and perspectives on materials-based hydrogen storage solutions: A critical review. *Int J Hydrogen Energ* 2017;42:289-311.
- [6] Phillips R, Dunnill Charles W. Zero Gap Alkaline Electrolysis Cell Designs for Renewable Energy Storage as Hydrogen Gas. *RSC Adv* 2016;6:100643-51.
- [7] Phillips R, Edwards A, Rome B, Jones DR, Dunnill Charles W. Minimising the ohmic resistance of an alkaline electrolysis cell through effective cell design. *Int J Hydrogen Energ* 2017;42:23986-94.

- [8] Gannon WJF, Jones DR, Dunnill Charles W. Enhanced Lifetime Cathode for Alkaline Electrolysis Using Standard Commercial Titanium Nitride Coatings. *Processes* 2019;7:112-23.
- [9] Budt M, Wolf D, Span R, Yan J. A review on compressed air energy storage: Basic principles, past milestones and recent developments. *Appl Energy* 2016;170:250–68.
- [10] Wang J, Lu K, Ma L, Wang J, Dooner M, Miao S, et al. Overview of Compressed Air Energy Storage and Technology Development. *Energies* 2017;10:991-1012.
- [11] Zhou Q, Du D, Lu C, He Q, Liu W. A review of thermal energy storage in compressed air energy storage system. *Energy* 2019;188:115993.
- [12] Hesse HC, Schimpe M, Kucevic D, Jossen A. Lithium-Ion Battery Storage for the Grid—A Review of Stationary Battery Storage System Design Tailored for Applications in Modern Power Grids. *Energies* 2017;10:2107-48.
- [13] Akinyele D, Belikov J, Levron Y. Battery Storage Technologies for Electrical Applications: Impact in Stand-Alone Photovoltaic Systems. *Energies* 2017;10:1760-98.
- [14] Martinez-Bolanos JR, Udaeta MEM, Gimenes ALV, da Silva VO. Economic feasibility of battery energy storage systems for replacing peak power plants for commercial consumers under energy time of use tariffs. *J Energy Storage* 2020;29:101373.
- [15] Alagoz BB, Kaygusuz A, Karabiber A. A user-mode distributed energy management architecture for smart grid applications. *Energy* 2012;44:167-77.
- [16] Tervo E, Agbim K, DeAngelis F, Hernandez J, Kim HK, Odukomaiya A. An economic analysis of residential photovoltaic systems with lithium ion battery storage in the United States. *Renew Sust Energ Rev* 2018;94:1057–66.
- [17] Jing W, Lai CH, Wong WSH, Wong MLD. Dynamic power allocation of battery-supercapacitor hybrid energy storage for standalone PV microgrid applications. *Sustain Energy Technol Assess* 2017;22:55–64.
- [18] Vega-Garita V, Ramirez-Elizondo L, Narayan N, Bauer P. Integrating a photovoltaic storage system in one device: A critical review. *Prog Photovolt Res Appl* 2019;27(4):346-70.
- [19] Liu R, Liu Y, Zou H, Song T, Sun B. Integrated solar capacitors for energy conversion and storage. *Nano Res* 2017;10(5):1545–59.
- [20] Meng H, Pang S, Cui G. Photo-Supercapacitors Based on Third-Generation Solar Cells. *ChemSusChem* 2019;12:3431–47.
- [21] Ng CH, Lim HN, Hayase S, Harrison I, Pandikumar A, Huang NM. Potential active materials for photo-supercapacitor: A review. *J Power Sources* 2015;296:169-85.
- [22] Das A, Ojha M, Subramanyam P, Deepa M. A poly(3,4-propylenedioxythiophene)/carbon micro-sphere-bismuth nanoflake composite and multifunctional Co-doped graphene for a benchmark photo-supercapacitor. *Nanoscale Adv* 2020;2:2925–42.
- [23] Das A, Deshagani S, Ghosal P, Deepa M. Redox active and electrically conducting cobalt telluride Nanorods/Poly(1-aminoanthraquinone) composite and photoactive Rose Bengal dye based photo-supercapacitor. *Appl Mater Today* 2020;19:100592.
- [24] Xu J, Ku Z, Zhang Y, Chao D, Fan HJ. Integrated Photo-Supercapacitor Based on PEDOT Modified Printable Perovskite Solar Cell. *Adv Mater Technol* 2016;1:1600074.
- [25] Liu Z, Zhong Y, Sun B, Liu X, Han J, Shi T, et al. Novel Integration of Perovskite Solar Cell and Supercapacitor Based on Carbon Electrode for Hybridizing Energy Conversion and Storage. *ACS Appl Mater Interfaces* 2017;9:22361–8.
- [26] Li C, Islam MM, Moore J, Sleppy J, Morrison C, Konstantinov K, et al. Wearable energy-smart ribbons for synchronous energy harvest and storage. *Nature Communications* 2016;7:13319.

- [27] Jones DR, Phillips R, Gannon WJF, Rome B, Warwick MEA, Dunnill Charles W. Photocapacitive CdS/WO_x nanostructures for solar energy storage. *Sci Rep* 2019;9:11573.
- [28] Low J, Jiang C, Cheng B, Wageh S, Al-Ghamdi AA, Yu J. A Review of Direct Z-Scheme Photocatalysts. *Small Methods* 2017;1:1700080.
- [29] Wang Y, Song Y, Xia Y. Electrochemical capacitors: mechanism, materials, systems, characterization and applications. *Chem Soc Rev* 2016;45:5925-50.
- [30] Shao Y, El-Kady MF, Sun J, Li Y, Zhang Q, Zhu M, et al. Design and Mechanisms of Asymmetric Supercapacitors. *Chem Rev* 2018;118:9233-80.
- [31] Da Silva LM, Cesar R, Moreira CMR, Santos JHM, De Souza LG, Pires BM, et al. Reviewing the fundamentals of supercapacitors and the difficulties involving the analysis of the electrochemical findings obtained for porous electrode materials. *Energy Storage Mater* 2020;27:555-90.
- [32] Wang G, Ling Y, Wang H, Yang X, Wang C, Zhang JZ, et al. Hydrogen-treated WO₃ nanoflakes show enhanced photostability. *Energy Environ Sci* 2012;5:6180-7.
- [33] Fernández-Domene RM, Sánchez-Tovar R, Lucas-Granados B, García-Antón J. Improvement in photocatalytic activity of stable WO₃ nanoplatelet globular clusters arranged in a tree-like fashion: Influence of rotation velocity during anodization. *Appl Catal B* 2016;189:266-82.
- [34] Hill JC, Choi K-S. Effect of Electrolytes on the Selectivity and Stability of n-type WO₃ Photoelectrodes for Use in Solar Water Oxidation. *J Phys Chem C* 2012;116:7612-20.
- [35] Vicentini R, Da Silva LM, Cecilio Junior EP, Alves TA, Nunes WG, Zanin H. How to Measure and Calculate Equivalent Series Resistance of Electric Double-Layer Capacitors. *Molecules* 2019;24:1452-60.
- [36] Nightingale ER. Phenomenological Theory of Ion Solvation. *J Phys Chem* 1959;63:1381-7.
- [37] Li K, Shao Y, Liu S, Zhang Q, Wang H, Li Y, et al. Aluminum-Ion-Intercalation Supercapacitors with Ultrahigh Areal Capacitance and Highly Enhanced Cycling Stability: Power Supply for Flexible Electrochromic Devices. *Small* 2017;13:1700380.
- [38] Pal B, Yang S, Ramesh S, Thangadurai V, Jose R. Electrolyte selection for supercapacitive devices: a critical review. *Nanoscale Adv* 2019;1:3807-35.
- [39] Barzegar F, Momodu DY, Fashedemi OO, Bello A, Dangbegnon JK, Manyala N. Investigation of different aqueous electrolytes on the electrochemical performance of activated carbon-based supercapacitors. *RSC Adv* 2015;5:107482-7.
- [40] Wang Y, Yuan A, Wang X. Pseudocapacitive behaviors of nanostructured manganese dioxide/carbon nanotubes composite electrodes in mild aqueous electrolytes: effects of electrolytes and current collectors. *J Solid State Electrochem* 2008;12:1101-7.
- [41] Jitvisate M, Seddon JRT. Direct Measurement of the Differential Capacitance of Solvent-Free and Dilute Ionic Liquids. *J Phys Chem Lett* 2018;9:126-31.
- [42] May S. Differential capacitance of the electric double layer: mean-field modeling approaches. *Curr Opin Electrochem* 2019;13:125-31.
- [43] Goodwin ZAH, Feng G, Kornyshev AA. Mean-Field Theory of Electrical Double Layer In Ionic Liquids with Account of Short-Range Correlations. *Electrochim Acta* 2017;225:190-7.
- [44] Zhan C, Lian C, Zhang Y, Thompson MW, Xie Y, Wu J, et al. Computational Insights into Materials and Interfaces for Capacitive Energy Storage. *Adv Sci* 2017;4:1700059.
- [45] Bo Z, Li C, Yang H, Ostrikov K, Yan J, Cen K. Design of Supercapacitor Electrodes Using Molecular Dynamics Simulations. *Nano-Micro Lett* 2018;10:33-55.
- [46] Wu P, Huang J, Meunier V, Sumpter BG, Qiao R. Voltage Dependent Charge Storage Modes and Capacity in Subnanometer Pores. *J Phys Chem Lett* 2012;3:1732-7.

- [47] Laheäär L, Przygocki P, Abbas Q, Béguin F. Appropriate methods for evaluating the efficiency and capacitive behavior of different types of supercapacitors. *Electrochem Commun* 2015;60:21–5.
- [48] Gelderman K, Lee L, Donne SW. Flat-Band Potential of a Semiconductor: Using the Mott–Schottky Equation. *J Chem Educ* 2007;84(4):685-8.
- [49] Taylor SR, Gileadi E. Physical Interpretation of the Warburg Impedance. *Corros Sci* 1995;51(9):664-71.
- [50] Hankin A, Bedoya-Lora FE, Alexander JC, Regoutz A, Kelsall GH. Flat band potential determination: avoiding the pitfalls. *J Mater Chem A* 2019;7:26162-76.
- [51] Uosaki K, Kita H. Effects of the Helmholtz Layer Capacitance on the Potential Distribution at Semiconductor/Electrolyte Interface and the Linearity of the Mott-Schottky Plot. *J Electrochem Soc* 1983;130(4):895-7.
- [52] Nguyen TQ, Breitkopf C. Determination of Diffusion Coefficients Using Impedance Spectroscopy Data. *J Electrochem Soc* 2018;165(14):E826-E31.
- [53] Levi MD, Aurbach D. Impedance of a Single Intercalation Particle and of Non-Homogeneous, Multilayered Porous Composite Electrodes for Li-ion Batteries. *J Phys Chem B* 2004;108:11693-703.
- [54] Mohamedi M, Takahashi D, Uchiyama T, Itoh T, Nishizawa M, Uchida I. Explicit analysis of impedance spectra related to thin films of spinel LiMn_2O_4 . *J Power Sources* 2001;93:93-103.
- [55] Huang J, Li Z, Liaw BY, Zhang J. Graphical analysis of electrochemical impedance spectroscopy data in Bode and Nyquist representations. *J Power Sources* 2016;309:82-98.
- [56] Levi MD, Lu Z, Aurbach D. Application of finite-diffusion models for the interpretation of chronoamperometric and electrochemical impedance responses of thin lithium insertion V_2O_5 electrodes. *Solid State Ion* 2001;143:309-18.
- [57] Oldenburger M, Bedürftig B, Gruhle A, Grimsmann F, Richter E, Findeisen R, et al. Investigation of the low frequency Warburg impedance of Li-ion cells by frequency domain measurements. *J Energy Storage* 2019;21:272–80.
- [58] Cruz-Manzo S, Greenwood P. An impedance model based on a transmission line circuit and a frequency dispersion Warburg component for the study of EIS in Li-ion batteries. *J Electroanal Chem* 2020;871:114305.
- [59] Cruz-Manzo S, Greenwood P. Frequency Transition from Diffusion to Capacitive Response in the Blocked-Diffusion Warburg Impedance for EIS Analysis in Modern Batteries. *J Electrochem Soc* 2020;167:140507.
- [60] Mishra GK, Kant R. Modular theory for DC-biased electrochemical impedance response of supercapacitor. *J Power Sources* 2020;473:228467.
- [61] Huang J. Diffusion impedance of electroactive materials, electrolytic solutions and porous electrodes: Warburg impedance and beyond. *Electrochim Acta* 2018;281:170-88.